LAWRENCE
LIVERMORE
NATIONAL
LABORATORY

UCRL-JRNL-229290

Improvements In Mixing Time And Mixing Uniformity In Devices Designed For Studies Of Protien Folding Kinetics

S. Yao, O. Bakajin

March 22, 2007

Analytical Chemistry

Disclaimer

Improvements in mixing time and mixing uniformity in devices designed for studies of protein folding kinetics

*Shuhuai Yao and Olgica Bakajin**

Chemistry Materials & Life Sciences Directorate, Lawrence Livermore National Laboratory, Livermore, California 94550

yao4@llnl.gov, bakajin1@llnl.gov

*Corresponding Author: (email) bakajin1@llnl.gov; (phone) 925-422-0931; (fax) 925-423-0579.

ABSTRACT

We demonstrate a mixing time of 1 ± 1 μs with sample consumption of femtomoles in a microfluidic laminar flow mixer designed for studies of protein folding kinetics. Two limitations of the previously proposed designs are addressed: 1) the shape of the photolithographically defined mixing region that limits mixing uniformity and 2) the formation of Dean vortices at high flow rates which limits the mixing time. We address these two problems in two individual designs by introducing shape-optimized nozzles and reduced side channel curvatures,

respectively. The final design that combines both of these features achieves optimized performance. We quantified the mixing performance of these four designs by numerical simulation of coupled Navier-Stokes and convection-diffusion equations, and experiments using fluorescence resonance energy-transfer (FRET)-labeled DNA.

INTRODUCTION

Many proteins fold through transient intermediates that are populated in the submillisecond time regime [(1)]. These early events are crucial for understanding how protein folding is initiated and directed along specific pathways, and have been a major focus of recent experimental [(2)-5] and theoretical work [(6)-9]. Molecular dynamics (MD) simulations of protein folding will be essential for our understanding of folding since they will be able to offer an insight into fast folding kinetics. However, they are currently still of limited value, requiring on the order of several months per microsecond [(10)] of computational time on the fastest supercomputers. Although experimental methods such as laser-based photochemical triggering and temperature/pressure jump techniques offer time resolution in nanoseconds, they are not the most general techniques for the initiation of the protein folding reaction. Ultrarapid mixing methods in which the chemical denaturant is diluted are advantageous because they generate a large thermodynamic perturbation on most biomolecular systems [(11)] and therefore are the most versatile and generally applicable method of initiating chemical and biological processes [(12)]. New experimental approaches are starting to access time scales from microseconds to milliseconds [11-16].

The fundamental process that leads to complete mixing of two solutions at the molecular level is diffusion. Since the diffusion time scales as the square of the diffusion length, for typical small molecule solutes (e.g., D = 1e-9 m^2/s) the length scale for diffusion needs to be reduced to

as little as 30 nm to achieve microsecond mixing. Turbulent mixers that break the flow in small eddies have been used to accelerate mixing. Since turbulence occurs at high Reynolds numbers, high flow rates lead to extreme sample consumption. As an alternative to turbulent mixing, hydrodynamic focusing (lamination) first proposed by Brody et al. [(17)] has opened new windows to achieve rapid mixing with minimal sample consumption. Hydrodynamic focusing mixers have been developed by Knight et al. [(18)] and optimized by Hertzog et al. [(16)], in which the buffer solutions from two symmetric orthogonal side channels focus the sample solutions from the center channel into a thin stream that can be as small as 50 nm [(18)]. The fastest mixing time has been reported as 8 μs [(16)] and 4 μs [(19)] with femtomole sample consumption. Recently, Park et al. [(20)] demonstrated a five-inlet port mixer that incorporates the sheath flow from the two diagonal channels as a barrier between solutions flowing from the center and the two side channels during the focusing process. Using this scheme the width of the focused jet is effectively reduced by the sheath flow instead of relying on the small nozzles or channels. In a parallel effort, Pabit and Hagen [(11)] constructed a laminar coaxial jet mixer from fused silica capillary of inner diameter 20 μm that allows UV-excited fluorescence measurements with ~ 400 μs dead time. Sundararajan et al. [(21)] presented a generalization of the conventional 2D hydrodynamic focusing to 3D. 3D hydrodynamic focusing offers the advantages of precision position of sample flow to the center of the channel in both vertical and lateral dimensions. Multilayer micromolding procedures were used to fabricate 3D microfluidic structures with polydimethylsiloxane (PDMS). Hydrodynamic focusing mixers have been successfully used in protein and RNA folding studies, combined with detection methods of FRET [(16)], small-angle X-ray scattering (SAXS) [(22), (23)], Fourier transform IR (FTIR) spectroscopy [(24)], and UV fluorescence spectroscopy [(11), (25)]. Hydrodynamic focusing is

also an effective method in flow cytometry [(26), (27)], cell patterning [(28)-(30)], liposome formation [(31)], rapid cell lyses [(32)], surface chemical modification [(33), (34)], DNA self-assembly and sequencing [(35), (36)].

The continued improvement of laminar mixing techniques remains an important avenue toward progress in protein folding kinetic studies. This paper discusses the limitations of the previous designs and our solutions to these limitations. First, as pointed before by Hertzog et al. [(19)] and Park et al. [(20)], the premature mixing prior to formation of the focused jet, referred to as "premixing" causes a variation in the degree of mixing for each individual streamline originated from the center channel [(20)]. This mixing uniformity is limited by the size of the nozzle, typically >1 μm in photolithography. Second, the higher flow rate desired to achieve fast mixing induces 3D effects, which limit mixer performance. The 3D effects, referred to as Dean vortices, are formed in curved channels when inertial effects of the fluid become significant. They occur because the faster moving fluid near the inner walls of the channel has larger centripetal acceleration than the slower moving fluid near the outer walls. The centripetal acceleration creates off-axis pressure gradients and velocities resulting in vortices in the cross-sectional plane. Consequently, under those conditions in a laminar flow mixer, the sample coming from the center channel no longer stays confined to a thin jet. We refer to this phenomenon as "jet splitting" further in the text. Since the sample molecules do not follow trajectories in the same horizontal plane of the channel, it becomes difficult to estimate the flow velocities along these streamlines. More importantly, the 3D effects introduce vastly different flow velocities for the different streamlines, which introduce large variation in the time history of different streamlines.

In this study, we addressed these two problems in two individual designs with shape-optimized nozzles and reduced channel curvatures, respectively. The final design that achieves best performance combines both of these features. We quantified the mixing performance of these four designs by numerical simulation of coupled Navier-Stokes and convection-diffusion equations, and experiments measuring the collapse of FRET-labeled single-strand-DNA (ssDNA) in confocal scanning microscopy. In particular, the jet splitting issue associated with Dean vortex flow was investigated in 3D simulation and cross-sectional confocal scans. With our final optimized design, we improved the mixing uniformity across the streamlines prior to the jet formation as well as reduced the mixing time by increasing the local velocity in the mixing regime and the total absolute flow rate in the mixer.

EXPERIMETNAL DETAILS

Mixer Design and Operation

We investigated four mixer designs in this study. Figure 1 shows the bright-field reflection CCD images of the mixing regions for the four designs in this study. Mixer 1, whose mixing region is a simple cross, is the original design [(16)]. Mixer 2 has a smaller nozzle shape in the mixing region after the cross resulting in a narrower focused "neck" region before the jet forms and increased local flow velocities [(19)]. Mixer 3 has reduced curvatures from the side channels to the exit channel. Mixer 4 combines the features of mixers 2 and 3. The first two mixer designs have been studied by Hertzog et al. [(16), (19)]. The silicon-glass devices were fabricated using hard contact photolithography, deep reactive ion etching (DRIE), and anodic bonding [(16)]. The nozzles of the center and side channels are 1 μm wide (the photolithographically limited feature size). The widths of exit channels are 10 μm and all the

channel depths are 10 μm. The devices have on-chip filters that are made of arrays of posts with 1-2 μm spacing in each channel before the mixing region. All the devices have similar layouts with extended channels to inlets and outlets for fluid delivery. Each device is fabricated on a 1.5 x 1.5 x 0.07 cm die. In operation, the die is assembled to an acrylic housing via O-rings, where the fluid reservoirs are pressurized through the pneumatic lines. The pressures of center and side channels are controlled by two pressure regulators with 0-100 psi range and 0.1 % accuracy (Marsh-Bellofram, Inc., Newell, WV) and interfaced by a custom-built Labview program (National Instruments, Austin, TX). The flow resistances in all the devices was verified in micro-PIV measurements by Hertzog et al. [(16)] to agree within 95% accuracy with the analytical model.

FRET-labeled single-strand DNA

DNA oligonucleotide was purchased from Integrated DNA technologies, Inc. (Coralville, IA). The fragments are labeled with amine-reactive Carboxy tetramethyl-rhodamine (TAMRA) at the 3' end of the $(dT)_{39}$ and Alexa Fluor 647 NHS ester at the 5' end. The samples were purified by dual high-pressure liquid chromatography (HPLC). 100nM ssDNA solutions were mixed with 2 M NaCl to characterize the mixing time for all the mixers. NaCl solutions with concentration from 0 M to 3 M were used in equilibrium calibration for the FRET proximity ratio (*PR*) versus [NaCl]. All the solutions were prepared in 10 mM Tris-HCl buffer at pH 8 (Sigma-Aldrich Louis, MO) and the buffer solutions were filtered with 0.1 μm-pore diameter filter prior to use.

Confocal Scanning Microscopy

Fluorescence images were acquired using confocal scanning microscopy. A multiline CW argon ion laser (Coherent Inc., Santa Clara, CA) provides excitation at 488 nm or 514 nm through an inverted microscope (Eclipse TE300, Nikon) with a 60x/1.2 NA water immersion objective. Fluorescence emission was collected with the same objective, and passed through a dichroic mirror, and a 50 □m pinhole (Newport Co., Irvine, CA). For a single fluorescent image (e.g., dye quenching experiment), the signals were detected with an avalanche photodiode (APD, PerkinElmer Optoelectronics, Fremont, CA). For FRET measurements of ssDNA (with TAMRA and Alexa Fluor 647 as the donor and the acceptor, respectively), the emissions from the donor and acceptor were split by a 630DRLP dichroic mirror (DM, Omega Optical, Inc., Brattleboro, VT). The donor and acceptor signals were then passed through 580DF60 and 670DF40 emission filters (DM, Omega Optical, Inc., Brattleboro, VT), and collected by two identical APDs, respectively. Confocal images were scanned by a nanometer-resolution, three-axis piezo-stage (Physik Instrument, Germany) with custom software developed in Labview (National Instruments, Austin, TX). With laser excitation intensity of 5-10 μW, measured at the front focal plane of the objective where the specimen is located, the integration per pixel varied between 5 and 10 ms to leverage the signal-to-noise ratio. The cross-sectional profiles of the focused sample stream acquired by Z-scans (10 μm in width and 14 μm in depth) determine the flow conditions under which no jet splitting occurs and the vertical midplane of the channel where the flow can be approximated as two-dimensional laminar flow. Typical X-Y scans were 60 μm long (streamwise, X direction) and 8 μm wide (transverse, Y direction) and with 0.1 μm resolution in each direction. In FRET measurements, the proximity ratio (*PR*) along X direction was obtained by the background subtracted donor and acceptor image pairs. We extracted intensity versus X distance by averaging 0.5 μm wide in Y direction at 0.1 μm step in X direction centered along

the focused jet. The *PR* versus [NaCl] was calibrated in equilibrium measurements with pre-mixtures of ssDNA and NaCl solutions varied from 0 M to 3 M in the same experimental setup.

SIMULATION DETAILS

Numerical simulations were employed to quantify the mixing performance of these mixers (shown in Figure 1). The flow and concentration fields in these mixers are governed by the steady-state incompressible Navier-Stokes equation and the convective-diffusion equation for the faster diffusing reactant with lower Peclet number.

$$\rho(\vec{V}\cdot\nabla)\vec{V} = -\nabla P + \mu\nabla^2\vec{V} \qquad (1)$$

$$\nabla\cdot\vec{V} = 0 \qquad (2)$$

$$\vec{V}\cdot\nabla C = D\nabla^2 C \qquad (3)$$

Where $\vec{V}$ is the flow velocity, P is the pressure, ρ is the fluid density, μ is the dynamic viscosity. D and C are the diffusivity and the concentration of the reactant, respectively. For direct comparison with the experimental measurements of the collapse of FRET-labled ssDNA, we applied the appropriate fluid properties of aqueous solutions of NaCl in the control volume. The diffusivity of NaCl solution of 1.5e-9 m^2/s (less than 2% variation for 0-2M) [(37)] was used in our model. Since ρ and μ are approximately linearly dependent on the NaCl concentration [(38)], in the model, we used the following dependences (at 25ºC):

$$\rho = \rho_0(1 + 0.037 * C) \quad (0 \le C \le 2M) \qquad (4)$$

$$\mu = \mu_0(1 + 0.104 * C) \quad (0 \le C \le 2M) \qquad (5)$$

where ρ_0 (= 997 kg/m^3) and μ_0 (= 0.89 mPa·S) are the density and the dynamic viscosity for pure water at 25ºC.

The coupled equations 1-3 were numerically solved by a commercial program, Comsol Multiphysics (Comsol Inc., Stockholm, Sweden) with a finite element scheme.

Validation of laminar flow assumption

The flow field in a curved channel has been extensively studied [(39)-42]. When a fluid flows through a curved channel, at high enough flow rates steady laminar flow evolves into unstable secondary flows resulting in rotating spiral vortices (known as Dean's vortices) in the cross-sectional plane of the channel. Dean's vortices are a result of differential centrifugal forces acting on the fluid at the center and at the near-wall regions of the channel. In the center of the channel the axial (streamwise) velocities are greater than those near the walls. Therefore the fluid in the center is driven to the outside of the bend. Due to the constraint of fluid continuity, the flow returns along the walls to the inside of the bend. The Dean number is the nondimensional parameter that characterizes flow in curved channels. The Dean number *De* is defined as $De = Re\sqrt{d/R}$, where *Re* is the Reynolds number (ud/ν), *u* is the average velocity across the stream, *d* is the width of the channel, ν is the kinetic viscosity, and *R* is the radius of curvature. As the Dean number increases, so does the intensity of the secondary flow [(43)].

We employed 3D simulation of the governing equations (1-3) for a curved channel with geometry similar to the mixing region of mixers 1 and 3: 90° curved and 160° curved channels, respectively. The cross-sectional flow and concentration fields at x = 5 μm in the exit channel are shown in Figure 2. In the downstream channel where the flow is fully-developed, both vorticity and concentration decreased along the channel due to diffusion but the variation in flow and concentration profile were negligible. The total flow rate was gradually increased as indicated by the maximum flow velocity at exit, U_e. The flow ratio of the center inlet flow rate

to the side inlet flow rate, Q_c/Q_s, was kept at 0.02. In mixer 1 with side channels that come in at 90° the Dean vortices started to significantly affect the flow field in the cross-sections when the maximum velocity in the exit channel was greater than 1 m/s. The vorticity at U_e = 5 m/s was over 100 times higher than the vorticity at 1 m/s. The vortices in each quadrant were anti-symmetric to the central axes. The secondary flow in the vertical direction caused the jet to move to top and bottom of the channel and to finally split into two streams. In mixer 3, we reduced the curvature of the side channels with respect to the exit channel, and thus reduced the Dean's number by a factor of 2. The simulation results show that the jet splitting does not occur for U_e up to 5 m/s.

Use of 2D flow simulation in our analysis, that greatly reduces computational time, is justified under the conditions of no jet splitting and tightly focused jets. The optimized performance of each of the different designs is achieved at the highest flow rate at which the jet splitting still does not occur. Since the width of the focused jet is more than 10 times smaller than the channel depth, the flow at the vertical midplane can be approximated with 2D flow simulation.

Mixing performance quantification

The mixing time defined by Hertzog et al. [(16)] accounts for the time it takes for the reactant concentration in the center streamline to increase from 10 to 90 % of the initial concentration in the side channel. This definition may underestimate the mixing time due to the non-uniform mixing prior to the formation of the focused jet as the outermost streamline from the center channel starts to mix with the liquid from the side channel earlier than the center streamline. In a later paper [(19)], Hertzog et al. quantified this nonuniformity of mixing times by calculating the mixing time of all the streamlines across the focused stream and the standard deviation of these

mixing times. This phenomenon was also referred to as "premixing" by Park et al. [(20)]. To account for the non-uniform mixing, we considered variation across the 50 streamlines in the midplane originating from the center channel, where the sample molecules (e.g., protein, DNA) reside. Since the diffusivities of the Protein/DNA molecules are usually lower than that of the denaturant by a factor of 10, the sample molecules diffuse much slower and tend to remain on these streamlines from the center channel. As suggested by Hertzog et al. [(16)] and Park et al. [(20)], we define the mixing time as:

$$t_i(x) = \int_{x_0, C=0.01C_0}^{x} \frac{dx}{u_i(x)}$$

$$< t(x) >= \frac{\sum_i t_i(x) w_i(x)}{\sum_i w_i(x)}$$

And standard deviation of the mixing time as:

$$\sigma(x) = \sqrt{\frac{\sum_i (t_i(x) - < t(x) >)^2 w_i(x)}{\sum_i w_i(x)}} \qquad (t_i \geq 0)$$

where w_i is the width of the i^{th} streamline and the clock of the elapsed time t_i starts when the reactant concentration in the i^{th} streamline has increased to 1% of the initial concentration in the side channel, C_0. The final concentration regarded as fully mixed is arbitrary. For most of the protein folding studies, denaturant concentration changes higher than 70% fully trigger the folding process. Therefore, in this study, we consider 80% change. To evaluate the mixing performance, we define and use throughout this paper the *mixing time* as the average time <*t*> across the streamlines and consider the standard deviation σ in time as the figure of merit for the mixing uniformity.

RESULTS

Comparison of simulation results for 4 mixer designs

To illustrate the performance improvements in terms of mixing time and mixing uniformity for mixers 2-4 over mixer 1, we compare simulation results for the four mixers at the same flow conditions in Figure 3. For this comparison we chose the maximum flow of 0.5 m/s in the exit channel, conditions at which Dean vortices do not form for either of the designs. Mixers 2 and 4 reduce the mixing time by a factor of 3 compared to mixers 1 and 3. This reduction in mixing time is due to the increase in the local velocity in the mixing region with shape-optimized nozzles. The standard deviation curves, which measure the mixing uniformity, first increase before formation of the focused jets due to the speed variation across the streamlines originating from the center channels, and then plateau when the jets are narrowly focused near the center streamline in the exit channel. The plateaus indicate the overall variance in the mixing time. Mixers 2-4 all show improvement in mixing uniformity reflected by the reduction of the standard deviation over that of mixer 1. The optimized design mixer 4 reduces the standard deviation by a factor of 6.

Investigation of 3D effects using confocal scanning of cross-sectional jet profile

To investigate the effects of the Dean votices and to determine the flow conditions under which each of the mixers operates without jet splitting, we obtained confocal scans of the cross sections of the exit channel. We increased the total flow rate while keeping the flow ratio of the center to side channel at 1:50, which is close to flow ratio at which the optimal mixing time is achieved [(16)]. A stream of 10 μM dextran-conjugated Alexa Fluor 488 (10 kDa) (Molecular Probes, Eugene, OR) was pressurized in the center channel and focused by 10 mM PBS buffer

(pH 7.4, Sigma-Aldrich Louis, MO) on both sides. The cross sectional profiles of the focused jet at the fixed detection location x = 50 μm are shown in Figure 4. The pseudo-color images show the concentration profiles of the focused fluorescent dye streams. The total flow rate is indicated by the maximum flow velocity at exit, U_e. At low flow rate (U_e is equal or less than 0.5 m/s, the total flow rate is 24 nl/s in a 10 x 10 μm channel), the cross-sectional focused stream profiles are spindle-like for all the mixers. As the flow rate increases, the cross-sectional jet profiles elongate in the vertical direction. As the effective velocities in the curved channels get higher, the Dean vortices in the cross-sectional planes cause significant secondary flow in the vertical direction. At that point, the high concentration stream moves towards the top and bottom of the channel, to finally split into two concentrated streams symmetrical in the midplane of the channel. These experimental observations qualitatively agree with the 3D simulation results as described in the Simulation Section. We observed obvious jet splitting in the focused streams at U_e = 2 m/s, 1 m/s, and 4 m/s for mixer 1, 2, and 4 respectively. Performance of mixer 3 in our setup was limited by the available pressure supply. From these results, we determined the flow velocities at exit for which the fastest mixing without jet splitting will occur: 1 m/s, 0.5 m/s, 5 m/s and 3 m/s for mixers 1-4 respectively. Since the jet splitting significantly lowers the fluorescent signal in the midplane, for the measurement of mixing time we choose to operate the mixers below these threshold flow conditions to achieve better signal-to-noise ratio.

We used the cross-sectional confocal scans of the channel homogenously filled with fluorescent dye solutions to determine the vertical midplane where the confocal scans of the focused jets in X-Y dimension should be taken for our mixing characterization experiments. We also used the cross-sectional scans taken at different detection points along the channel to insure that the device was held in a horizontal level for each experiment.

Measurement of mixing time using collapse of FRET-labeled ssDNA

To characterize the mixing response of our mixers, we performed FRET measurements of ssDNA (dT_{39}) collapsed by high concentration salt. FRET between donor and acceptor fluorophores is widely used to characterize the conformations and dynamics of biomolecules such as proteins. FRET can provide distance information for donor and acceptor pairs of points on the amino acid chain as a function of folding [(44)]. Characterization of mixing with a FRET assay is most desirable since our ultrafast continuous-flow mixers are designed for FRET-labeled protein assay. Murphy et al. [(45)] has estimated the persistence length of oligo-dT decreases with increasing salt concentration using FRET fluorescence spectroscopy. As described earlier, the ssDNA molecule is labeled with a dye molecule at each end. When the two dyes get closer, the FRET energy starts to transfer from the donor to the acceptor. This transfer of energy is irradiative, due primarily to a dipole-dipole interaction between donor and acceptor. The FRET proximity ratio, defined as $PR = I_A/(I_A + I_D)$, where I_A and I_D are the background corrected intensities of the emission of the acceptor and the donor, respectively, indicates the signal response of the concentration change upon mixing in the focused stream. The ssDNA molecules undergo sub-microsecond collapse upon transition from a low-concentration salt to a high-concentration salt environment. This collapse is faster than the mixer performance, so it allows for accurate mixer characterization.

The data was taken using 100nM ssDNA and 2M NaCl solutions that were pressurized into the center channel and the side channels respectively. The ssDNA molecules in the focused stream experienced a rise in salt concentration while flowing downstream due to the diffusion of NaCl . The data was taken at the vertical midplane of the channel with a confocal spot that measures

approximately 0.3 μm in the radial direction and 1 μm in the vertical direction. To achieve the minimum mixing time, we compared the mixing performance of each mixer at the highest flow rates without jet splitting and at their corresponding optimal flow ratio of the center inlet flow rate to the side inlet flow rate [(16)]. The flow conditions for each mixer are U_e = 1 m/s and Q_c/Q_s = 0.02 for mixer 1, U_e = 0.5 m/s and Q_c/Q_s = 0.04 for mixer 2, U_e = 5 m/s and Q_c/Q_s = 0.02 for mixer 3, and U_e = 3 m/s and Q_c/Q_s = 0.02 for mixer 4. The characterization results of [NaCl] vs. time for each mixer are shown in Figure 5 (circles). The results were obtained by averaging five measurements that were repeatable to within 5 %. We overlaid the numerical results (solid curve) with the experimental data. We converted the *PR* into [NaCl] with an equilibrium calibration curve (by measuring the FRET signals of premixed ssDNA and NaCl solution from 0-3 M in the same experimental setup in Figure S-1) so that we can compare the results with our simulated solute concentration. We estimated the concentration time history by converting the Eulerian space coordinate to Lagrangian time coordinate. The space-to-time conversion was obtained from the numerical simulation with space resolution of 0.05 μm as described in the Simulation Section (also shown in Figure S-2).

The measured mixing times, $\langle t \rangle$, for these four mixers are 22 ± 7 μs, 17 ± 7 μs, 4 ± 2 μs, and 1 ± 1 μs, respectively. The results agree well with the simulation data. The optimized design reduced the mixing time by at least an order of magnitude from the original design. Note that using the Lagrangian time history in the center streamline the mixing time in mixers 1 and 2 [16, 19] might have been underestimated by about a factor of 2.

We considered several sources that contributed to the uncertainty in mixing time. The alignment of the confocal images to the simulation coordinates is probably the most significant contribution of the errors. The simulated flow field used for time estimation has a steep gradient

in the mixing region within a few microns from the center nozzle exit. The diffraction limited confocal spot size limits the spatial resolution to about 0.3 μm. Misalignment of ± 0.3 μm along the channel results in 0.7-6.0 μs variation in the mixing time (different for different mixer designs). For the fastest mixing mixer, this variation is equivalent to the magnitude of the mixing time and limits our time resolution. The second source of error arises due to the uncertainty of the registration of the vertical midplane, which is limited by the size of the confocal spot in Z-direction. The flow speed in the planes that are ± 1 μm away from the vertical midplane is lower by less than 5 % than the maximum value. Thus an error is registration of the vertical midplane causes errors in measurement of the mixing time. As also discussed by Hertzog et al. [(19)], other instrumental errors including the accuracy of the applied pressure and the discrepancy in channel geometry due to variation of micro-fabrication will change the flow rate. The sensitivity to flow rate changes of up to 10 % can change the mixing time by 75 %. If the flow ratio Q_c/Q_s is changed by ± 10 %, we estimate that the mixing time changes by 0.1 to 1.1 μs in our experimental conditions. The image noise in the confocal detection system is nearly negligible. Finally the two-dimensional flow model is a good approximation of the full three-dimensional flow and concentration fields to within 95 % accuracy.

CONCLUSIONS & DISCUSSION

We have performed both three-dimensional numerical and scanning confocal studies to optimize mixing performance of the mixers that rely on hydrodynamic focusing. We demonstrated fast mixing on the order of 1 ± 1 μs with our optimized design with ssDNA consumption less than 1 nl/s (corresponding to less than 360 fM/hour) and maximum exit velocity of 3 m/s. The mixers were characterized using the collapse of FRET-labeled ssDNA

under the increase of salt concentration in the mixers. Our optimized design combines shape-optimized nozzles and curvature-reduced channels. The improvement in both mixing time and mixing uniformity was achieved by optimization of mixer shape. The shape-optimized nozzles increase the local speed in the mixing region. The more tightly focused region prior to the jet formation reduces the variation in mixing time for each streamline of the sample that originates from the center channel. Reduced curvature of the side channels enable the operating flow velocities of these mixers to increase by a factor of 5, thus also reducing the mixing time.

Room still exists for further improvements in the nozzle and channel geometry which would allow for higher flow rates without formation of Dean vortices. An alternative solution would be to use 3D hydrodynamic focusing either by a co-axial design [(11)] or by a 3D structure in which the jet is focused in both vertical and lateral dimensions [(21), (46)]. Although 3D microfabrication has been demonstrated by micromolding [(47)], laser machining [(48)], stereolithography [(49)] and two-photon lithography [(50)], reduction of the feature size to one micron or less in 3D structures still remains a challenge.

ACKNOWLEDGEMENT

We thank Dr. David Hertzog, Dr. Donald Sirbuly, and Avinash Kane of LLNL for their help in fabrication and experiments. We also thank our collaborators, Prof. Shimon Weiss' group at UCLA and Prof. Lisa Lapidus' group at MSU, for insightful discussion on protein folding kinetics and mixer design. We are grateful to Prof. Juan Santiago from Stanford University for helpful suggestions about the manuscript. This work was performed under the auspices of the U.S. Department of Energy under Contact W-7405-Eng-48 with funding from the LDRD program and partially supported by funding from NSF FIBR Grant 0623664 administered by the

Center for Biophotonics, an NSF Science and Technology Center, managed by the University of California, Davis, under Cooperative Agreement PHY 0120999.

SUPPORTING INFORMATION AVAILABLE

The supplementary information includes (1) a calibration plot of FRET proximity ratio (*PR*) versus sodium chloride concentration [NaCl] (Figure S-1). This curve is used to convert the measured FRET signals from the ssDNA collapse experiments to salt concentration. (2) The spatial-to-time conversion curves from simulation results (Figure S-2). Both figures are used for the final mixing time characterization curves in Figure 5.

Figure S-1. FRET proximity ratio (*PR*) signals of premixed ssDNA and NaCl solution from 0-3 M in equilibrium calibration measurements. The solid curve was obtained by fitting the data to a Boltzmann equation: $PR = 0.497 - 7.866 \Big/ (1 + e^{\frac{C+3}{0.934}})$ with nonlinear regression $R^2 = 0.997$.

Figure S-2. Simulation results of the elapsed time versus the distance from the nozzle for each mixer at the same flow conditions as described in Figure 5. The t (x) curves are used to convert the spatial coordinate in experimental data to the time coordinate. $t = 0$ is set when the [NaCl] starts increase, $C = 0.01\ C_0$.

FIGURE CAPTIONS

Figure 1. Bright-field images of the mixing regions for the four mixer designs. Mixer 1 whose mixing region is a simple cross is the original design. Mixer 2 has smaller width in the mixing region after the cross resulting in narrower focused jet and increased local flow velocities. Mixer 3 has reduced curvatures from the side channels to the exit channel. Mixer 4 combines the features of Mixers 2 and 3.

Figure 2. Numerical simulations of the cross-sectional flow and concentration fields in 90° curved (top row) and 160° curved (bottom row) channels, corresponding to the designs of mixer 1 and mixer 3, at U_e = 1 m/s and 5 m/s. At U_e = 5 m/s, mixer 1 shows jet splitting due to formation of Dean's vortices.

Figure 3. 2D simulation of mixing performance showing mixing time and uniformity improved by shape-optimized nozzles and reduced channel curvatures. The maximum flow is 0.5 m/s in the exit channel. The mixing times to achieve 80% change in concentration were obtained as $\langle t \rangle$ averaged over the streamlines from the center channel. For mixers 1-4 they are 44 μs, 15 μs, 40 μs, 11 μs, and the standard deviations σ that reflect the degree of mixing uniformity are 37 μs, 16 μs, 13 μs, 6 μs, respectively.

Figure 4. Confocal scans of cross-sectional jet profiles for the four mixers at different flow rates. Each image is 14 x 10 μm with 0.1 μm resolution in each dimension. Highlighted panels show the highest flow rate at which the jet splitting does not occur for each of the mixers.

Figure 5. Mixing time characterized by FRET-labeled ssDNA collapsed by high salt solutions. We compare the mixing time under the optimal conditions for each of the designs: the highest flow rate where jet splitting does not occur (observed from the cross-sectional scans of the jet profiles) and their corresponding optimal flow ratio of the center inlet flow rate to the side inlet

flow rate to achieve the minimum mixing time [(16)]. The flow conditions for each mixer are U_e = 1 m/s and Q_c/Q_s = 0.02 for mixer 1, U_e = 0.5 m/s and Q_c/Q_s = 0.04 for mixer 2, U_e = 5 m/s and Q_c/Q_s = 0.02 for mixer 3, and U_e = 3 m/s and Q_c/Q_s = 0.02 for mixer 4. The data represents an average of five measurements. Numerical simulation results are overlaid as a solid curve.

REFERENCES

(1) Bilsel, O.; Kayatekin, C.; Wallace, L.; and Matthew, C.R. *Rev. Sci. Instrum.* **2005**, *76*, 014302.1-014302.7.

(2) Pryse, K. M.; Bruckman, T. G.; Maxfield, B. W.; Elson, E. L. *Biochem.* **1992**, *31*, 5127-5136.

(3) Hagen, S.J.; Eaton, W.A. *J. Mol. Biol.* **2000**, *301*, 1037-1045.

(4) Eaton W. A.; Munoz, V.; Hagen, S. J.; Jas, G. S.; Lapidus, L. J.; Henry, E. R.; Hofrichter, *J. Annu. Rev. Biophys. Biomol. Struct.* **2000**, *29*, 327-359.

(5) Roder, H. *Proc. Natl. Acad. Sci. U.S.A.* **2004**, *101*, 1793-1794.

(6) Sali, A.; Shakhnovich, E.I.; Karplus, M. *J. Mol. Biol.* **1994**, *235*, 1614-1636.

(7) Dill, K.A.; Bromberg, S.; Yue.; Fiebig, K.M.; Yee, D.P.; Thomas, P.D.; Chan, H.S. *Protein Sci* **1995**, *4*, 561-602.

(8) Pande, V. S.; Baker, I.; Chapman, J.; Elmer, S. P.; Khaliq, S.; Larson, S. M.; Rhee, Y. M.; Shirts, M. R.; Snow, C.; Sorin, E.; Zagrovic, B. *Biopolymers* **2003**, *68*, 91-109.

(9) Swope, W.C.; Pitera, J.W.; Suits, F.J. *J. Phys. Chem. B* **2004**, *108*, 6571–6581.

(10) Snow, C.D.; Sorin, E.J.; Rhee, Y.M.; Pande, V.S. *Annu. Rev. Biophys. Biomol. Struct.* **2005**, *34*, 43–69.

(11) Pabit, S.A.; Hagen, S.J. *Biophys. J.* **2002**, *83*, 2872-2878.

(12) Shastry, M.C.R.; Luck, S.D.; Roder, H. *Biophys. J.* **1998**, *74*, 2714-2721.

(13) Chan, C.-K.; Hu, Y.; Takahashi, S.; Rousseau, D.L.; Eaton, W.A. *Proc. Natl. Acad. Sci. U.S.A.* **1997**, *94*, 1779-1784.

(14) Akiyama, S.; Takahashi, S.; Kimura, T.; Ishimori, K.; Morishima, I.; Nishikawa, Y.; Fujisawa, T. *Proc. Natl. Acad. Sci. U.S.A.* **2002**, *99*, 1329-1334.

(15) Roder, H.; Maki, K.; Cheng, H.; Shastry, M.C.R. *Methods* **2004**, *34*, 15-27.

(16) Hertzog, D.E.; Michalet, X.; Jager, M.; Kong, X.; Santiago, J.G.; Weiss, S.;Bakajin, O. *Anal. Chem.* **2004**, *76*, 7169-7178.

(17) Brody, J.P.; Yager P.; Goldstein, R.E.; Austin, R.H. *Biophys. J.* **1996**, *71*, 3430-3441.

(18) Knight, J. B.; Vishwanath, A.; Brody, J. P.; Austin, R. H. *Phys. Rev. Lett.* **1998**, *80*, 3863-3866.

(19) Hertzog, D.E.; Ivorra, B.; Mohammadi, B.; Bakajin, O.; Santiago, J.G. *Anal. Chem.* **2006**, *78*, 4299 – 4306.

(20) Park, H.-Y.; Qiu, X.; Rhoades, E.; Korlach, J.; Kwok, L.W.; Zipfel, W.R; Webb, W.W.; Pollack, L. *Anal. Chem.* **2006**, *78*, 4465-4473.

(21) Sundararajan, N.; Pio, M.S.; Lee, L.P.; Berlin, A.A. *J. MEMS.* **2004**, *13*, 559-567.

(22) Pollack, L.; Tate, M.W.; Darnton, N.C.; Knight, J.B.; Gruner, S.M.; Eaton, W.A.; Austin, R. H. *Proc. Natl. Acad. Sci. U.S.A.* **1999**, *96*, 10115-10117.

(23) Pollack, L.; Tate, M.W.; Finnefrock, A.C.; Kalidas, C.; Trotter, S.; Darnton, N.C.; Lurio, L.; Austin, R.H.; Batt, C.A.; Gruner, S.M.; Mochrie, S.G. J. *Phys. Rev. Lett.* **2001**, *86*, 4962-4965.

(24) Kauffmann, E.; Darnton, N.C.; Austin, R.H.; Batt, C.; Gerwert, K. *Proc. Natl. Acad. Sci. U.S.A.* **2001**, *98*, 6646-6649.

(25) Lapidus, L.J.; Yao, S.; McGarruty, K.S.; Hertzog, D.E.; Tubman, E.; Bakajin, O. *Biophys. J.* **2007**, accepted.

(26) Scampavia, L.D.; Blankenstein, G.; Ruzicka, J.; Christian, G.D. *Anal. Chem.* **1995**, *67*, 2743-2749

(27) Watson, J.V. *Cytometry* **1999**, *38*, 2–14.

(28) Takayama, S.; McDonald, J.C.; Ostuni, E.; Liang, M.; Kenis, P.J.A.; Ismagilov, R.F.; Whitesides, G.M. *Proc. Natl. Acad. Sci. U.S.A.* **1999**, *96*, 5545–5548.

(29) Chiu, D.T.; Jeon, N.L.; Huang, S.; Kane, R.S.; Wargo, C.J.; Choi, I.S.; Ingber, D.E.; Whitesides, G.M. *Proc. Natl. Acad. Sci. U.S.A.* **2000**, *97*, 2408–2413.

(30) Walker, G.M; Ozers M.S.; Beebe, D.J. *Sens. Actuators B* **2004** *98*, 347–355.

(31) Jahn, A.; Vreeland, W.N.; Gaitan, M.; Locascio, .L.E. *J. Am. Chem. Soc.* **2004**, *126*, 2674-2675.

(32) Sethu, P.; Anahtar, M.; Moldawer, L.L.; Tompkins, R.G.; Toner, M. *Anal. Chem.* **2004**, *76*, 6247-6253.

(33) Kenis, P.J.A.; Ismagilov, R.F.; Takayama, S.; whitesides, G.M., *Acc. Chem. Res.* **2000**, 33, 841-847.

(34) Zhao,B.; Moore, J.S.; Beebe, D.J. *Science* **2001**, *291*, 1023-1026.

(35) Wong, P.K.; Lee, Y.-K.; Ho, C.-M. *J. Fluid Mech.* **2003**, *497*, 55–65.

(36) Otten, A.; Köster, S.; Struth, B.; Snigirevc, A.; Pfohl, T. *J. Synchrotron Rad.* **2005**, *12*, 745–750.

(37) Chang, Y.C.; Myerson, A.S. *AIChE J.* **1995**, *31*, 890-894.

(38) Fair, J.A.; Ozbek, H. *Viscosity and Density Tables of Sodium Chloride Solutions*, **1977**, Rep. DOE/TIC-11364, NTIS.

(39) Dean, W.R. *Philos. Mag.* **1927**, *4*, 208-223.

(40) Pratap, V.S.; Spalding, D.B. *Aero. Q.* **1975**, *26*, 219-228.

(41) Ghia, K.; Sokhey, *J. ASME J. Fluids Eng.* **1977**, *99*, 640-648.

(42) Berger, A.; Talbot, L.; Yao, L.-S. *Annu. Rev. Fluid Mech.* **1983**, *15*, 461-512.

(43) Vanka, S.P.; Luo. G.; Winkler, C.M. *AIChE J.* **2004**, *50*, 2359-2368.

(44) Laurence, T.A.; Kong, X.; Jäger, M.; Weiss, S. *Proc. Natl. Acad. Sci. U.S.A.* **2006**, *102*, 17348–17353.

(45) Murphy, M.C.; Rasnik, I.; Cheng, W.; Lohman T.M.; Ha, T. J. *Biophys. J.* **2004**, *86*, 2530-2537.

(46) Toepke, M.W.; Brewer, S.H.; Vu, D.M.; Rector, K.D.; Morgan, J.E.; Gennis, R.B.; Kenis, P.J.A.; Dyer, R.B. *Anal. Chem.* **2007**, *79*, 122-128.

(47) Anderson, J.R.; Chiu, D.T.; Jackman, R.J.; Cherniavskaya, O.; McDonald, J.C.; Wu, H.; Whitesides, S.H.; Whitesides, G.M. *Anal. Chem.* **2000**, *72*, 3158–3164.

(48) Mutapcic, E.; Iovenitti, P.; Hayes, J.P. *Int. J. Adv. Manuf. Technol.* **2006**, *30*, 1076-1083.

(49) Zhang, X.; Jiang, X.N.; Sun, C. *Sens. Actuators A*, **1999**, *77*, 149–156.

(50) Zhou, W., Kuebler, S.M.; Braun, K.L.; Yu, T.; Cammack, J.K.; Ober, C.K.; Perry, J.W.; Marder, S.R. *Science* **2002**, *296*, 1106–1106.

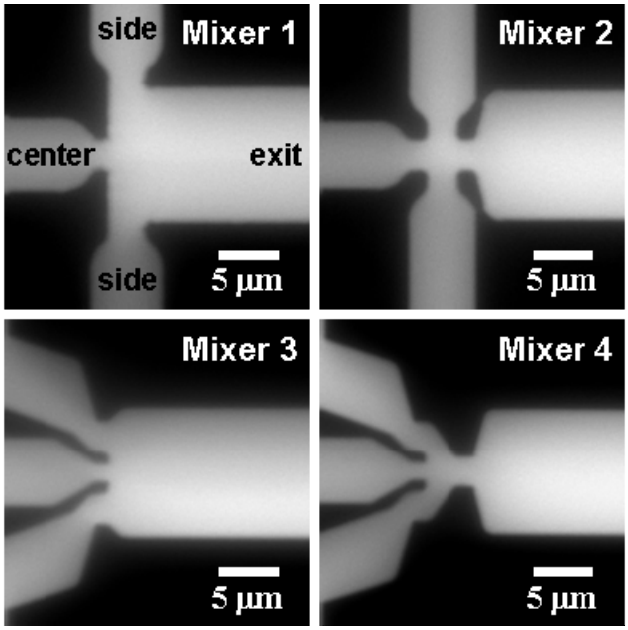

Figure 1. Bright-field images of the mixing regions for the four mixer designs. Mixer 1 whose mixing region is a simple cross is the original design. Mixer 2 has smaller width in the mixing region after the cross resulting in narrower focused jet and increased local flow velocities. Mixer 3 has reduced curvatures from the side channels to the exit channel. Mixer 4 combines the features of Mixers 2 and 3.

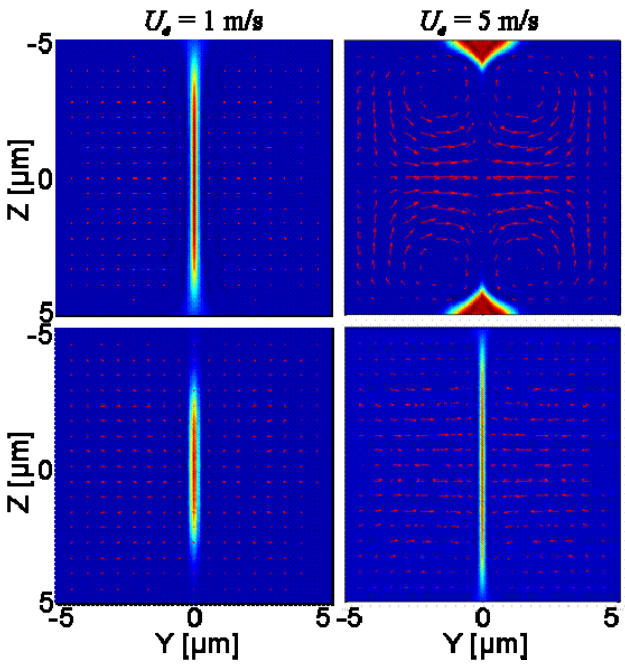

Figure 2. Numerical simulations of the cross-sectional flow and concentration fields in 90° curved (top row) and 160° curved (bottom row) channels, corresponding to the designs of mixer 1 and mixer 3, at U_e = 1 m/s and 5 m/s. At U_e = 5 m/s, mixer 1 shows jet splitting due to formation of Dean's vortices.

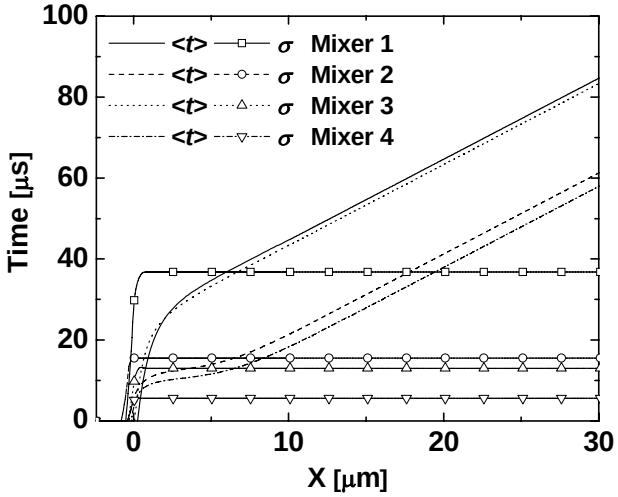

Figure 3. 2D simulation of mixing performance showing mixing time and uniformity improved by shape-optimized nozzles and reduced channel curvatures. The maximum flow is 0.5 m/s in the exit channel. The mixing times to achieve 80% change in concentration were obtained as $\langle t \rangle$ averaged over the streamlines from the center channel. For mixers 1-4 they are 44 μs, 15 μs, 40 μs, 11 μs, and the standard deviations σ that reflect the degree of mixing uniformity are 37 μs, 16 μs, 13 μs, 6 μs, respectively.

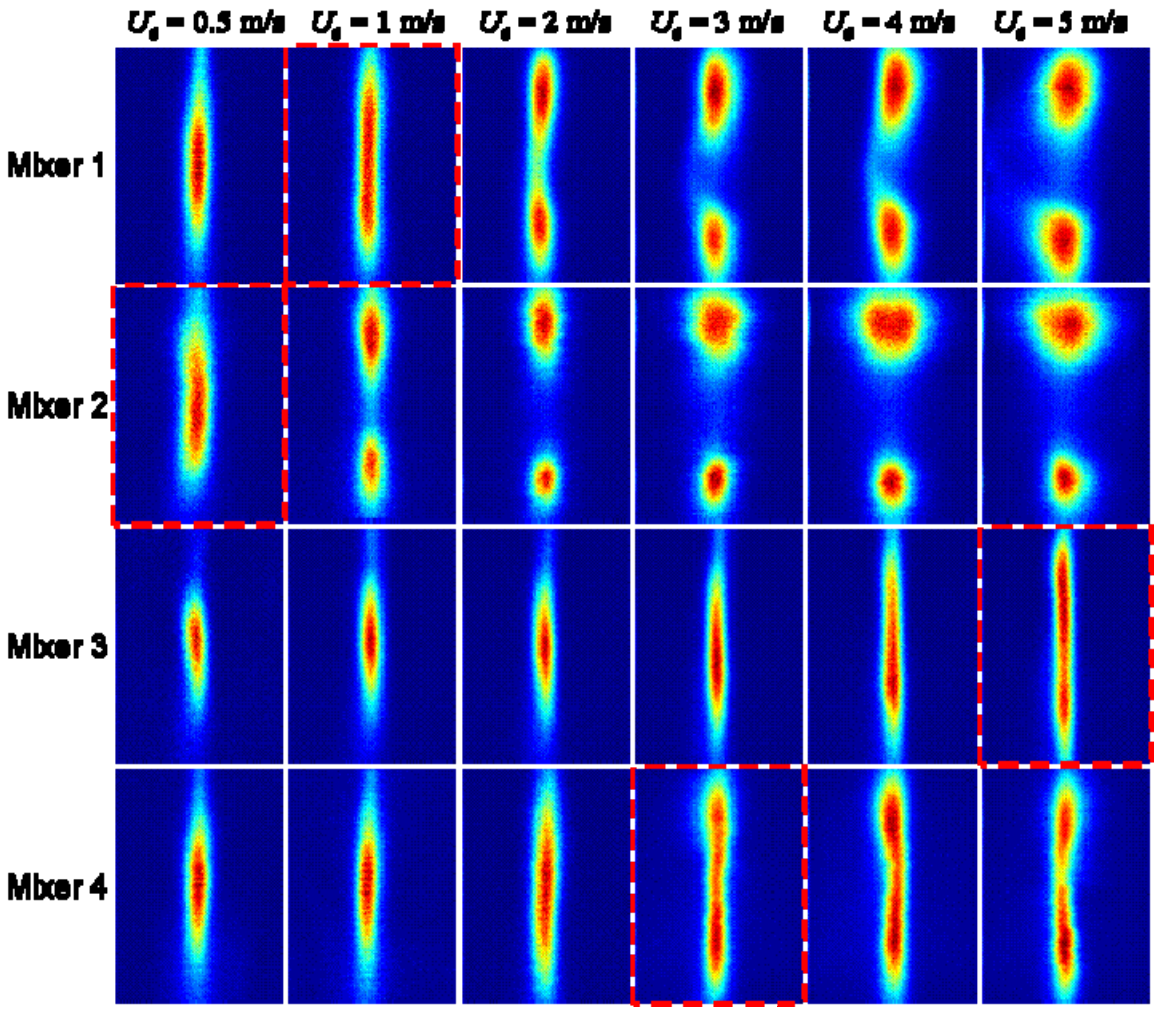

Figure 4. Confocal scans of cross-sectional jet profiles for the four mixers at different flow rates. Each image is 14 x 10 μm with 0.1 μm resolution in each dimension. Highlighted panels show the highest flow rate at which the jet splitting does not occur for each of the mixers.

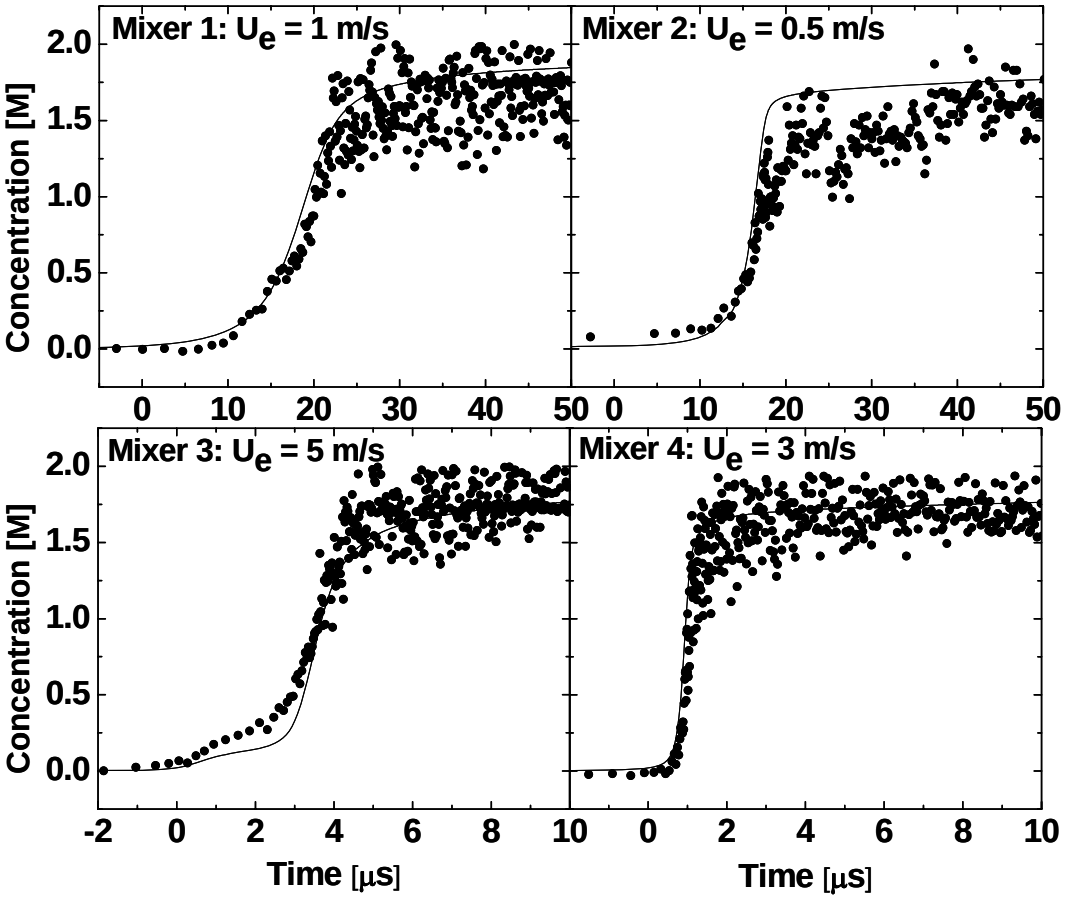

Figure 5. Mixing time characterized by FRET-labeled ssDNA collapsed by high salt solutions. We compare the mixing time under the optimal conditions for each of the designs: the highest flow rate where jet splitting does not occur (observed from the cross-sectional scans of the jet profiles) and their corresponding optimal flow ratio of the center inlet flow rate to the side inlet flow rate to achieve the minimum mixing time [(16)]. The flow conditions for each mixer are U_e = 1 m/s and Q_c/Q_s = 0.02 for mixer 1, U_e = 0.5 m/s and Q_c/Q_s = 0.04 for mixer 2, U_e = 5 m/s and Q_c/Q_s = 0.02 for mixer 3, and U_e = 3 m/s and Q_c/Q_s = 0.02 for mixer 4. The data represents an average of five measurements. Numerical simulation results are overlaid as a solid curve.

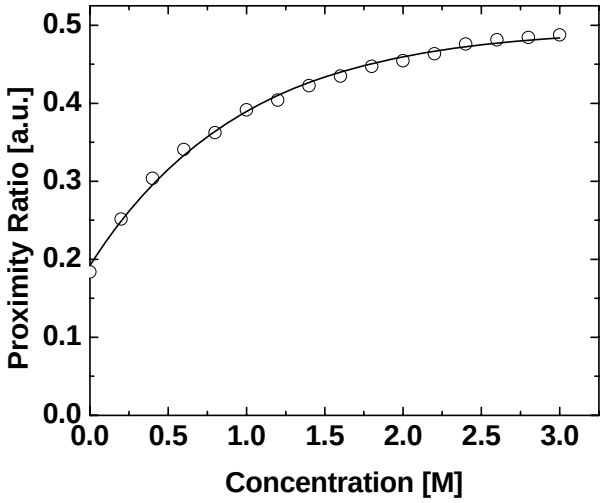

Figure S-1. FRET proximity ratio (*PR*) signals of premixed ssDNA and NaCl solution from 0-3 M in equilibrium calibration measurements. The solid curve was obtained by fitting the data to a Boltzmann equation: $PR = 0.497 - 7.866 / (1 + e^{\frac{C+3}{0.934}})$ with nonlinear regression $R^2 = 0.997$.

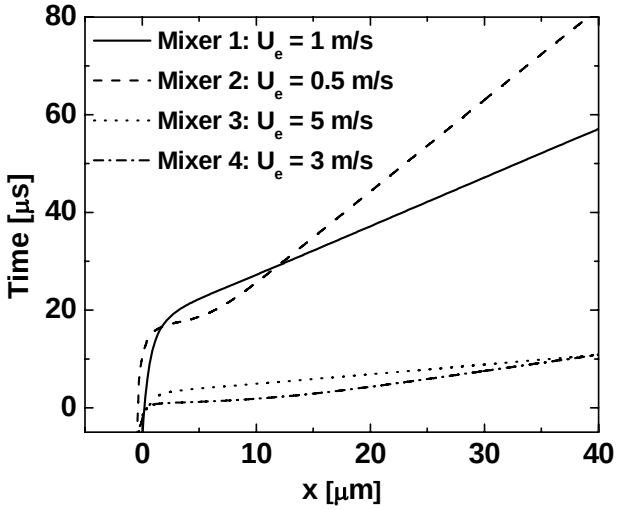

Figure S-2. Simulation results of the elapsed time versus the distance from the nozzle for each mixer at the same flow conditions as described in Figure 5. The t (x) curves are used to convert the spatial coordinate in experimental data to the time coordinate. $t = 0$ is set when the [NaCl] starts increase, $C = 0.01\ C_0$.